Journal of Materials Chemistry A

Accepted Manuscript

This article can be cited before page numbers have been issued, to do this please use: W. Zhang, X. Pan, P. Long, X. Liu, X. Long, Y. Yu and Z. Yi, *J. Mater. Chem. A*, 2017, DOI: 10.1039/C7TA04611A.

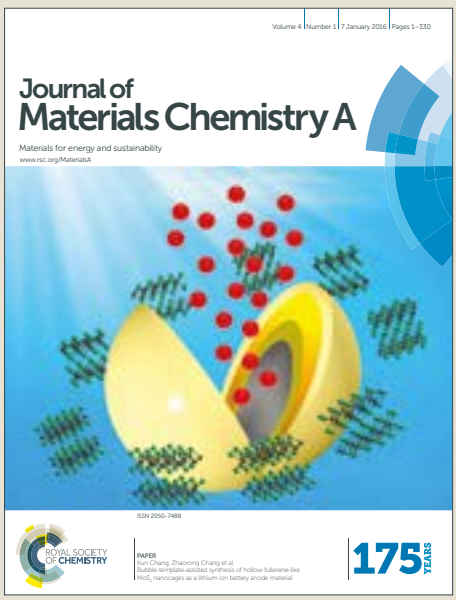

This is an Accepted Manuscript, which has been through the Royal Society of Chemistry peer review process and has been accepted for publication.

Accepted Manuscripts are published online shortly after acceptance, before technical editing, formatting and proof reading. Using this free service, authors can make their results available to the community, in citable form, before we publish the edited article. We will replace this Accepted Manuscript with the edited and formatted Advance Article as soon as it is available.

You can find more information about Accepted Manuscripts in the author guidelines.

Please note that technical editing may introduce minor changes to the text and/or graphics, which may alter content. The journal's standard Terms & Conditions and the ethical guidelines, outlined in our author and reviewer resource centre, still apply. In no event shall the Royal Society of Chemistry be held responsible for any errors or omissions in this Accepted Manuscript or any consequences arising from the use of any information it contains.

ROYAL SOCIETY OF CHEMISTRY

rsc.li/materials-a

View Article Online
DOI: 10.1039/C7TA04611A

Journal Name

ARTICLE

Platinum nanoparticles supported on defective tungsten bronze-type $KSr_2Nb_5O_{15}$ as novel photocatalyst for efficient ethylene oxidation†

Received 00th January 20xx,
Accepted 00th January 20xx

DOI: 10.1039/x0xx00000x

www.rsc.org/

Wei Zhang,[a,b] Xiaoyang Pan,[a] Peiqing Long,[a] Xitao Liu,[a] Xia Long,[a] Ying Yu,[b*] and Zhiguo Yi[a,c*]

Efficient separation and extraction of photo-induced carriers are crucial aspects of efficient semiconductor photocatalytic systems employed for photocatalytic oxidation (PCO) technology. In this study, Pt-loaded $KSr_2Nb_5O_{15}$ composite, as a novel photocatalyst, is reported for gaseous ethylene photo-oxidation, performing excellent PCO activity. Tungsten bronze-type $KSr_2Nb_5O_{15}$ (KSNO) with surface oxygen vacancies is prepared by a facile and low-cost molten salt synthesis method at 1200 °C for 6 h and a possible morphology evolution process was proposed. Pt was loaded on KSNO through a facile photodeposition method. The strong metal–support interaction (SMSI) between Pt nanoparticles and oxygen-deficient KSNO support is beneficial for superior photocatalytic efficiency and stability toward ethylene photo-oxidation. What's more, the structure and charge transfer path in the synthesized photocatalysts were investigated by X-ray photoelectron spectroscopy (XPS), high-resolution electron microscopy, and electron paramagnetic resonance (EPR).

1 Introduction

Ethylene (C_2H_4) as a volatile organic compound (VOC) has great influence on plant growth and the storage life of food.[1] Indeed, a small amount of ethylene can induce harmful reactions for the storage of fresh fruits and vegetables.[1] Therefore, the removal of trace amounts of ethylene is imperative. Heterogeneous photocatalytic oxidation (PCO) using semiconductors and solar energy is regarded as one of the most promising approaches to remove VOCs.[1-3] Under mild conditions, the PCO can degrade a broad range of contaminants into innocuous products such as CO_2 and H_2O without significant energy input.[2,3] Despite the promising future, this approach has faced a grand challenge in terms of reaction activity.[4]

In general, PCO process involves three key steps, that is, photo-induced carriers generation, transfer and consumption.[5] However, most photo-induced electron-hole pairs tend to recombine with each other before they diffuse to the active sites at semiconductor surface to initiate the PCO process, which causes the low PCO activity.[4-6] Therefore, it is important to develop strategies to separate electron-hole pairs and make them move to catalytically active sites at semiconductor surface. This means that the separation and extraction efficiency of photo-induced carriers are both great challenges to improve the PCO activity.

In order to promote the photo-induced carriers separation efficiency, various methods, such as p–n junctions, polymorph junctions and so on, have been proposed and put into practice, but the preparation process is generally intricate and the efficiency is still too low to separate electron-hole pairs completely during photocatalysis.[7-11] Recently, a new approach, utilizing materials that contain internal electric field, is proposed to promote the separation efficiency of photo-induced charge carriers.[7,8,12-17] It is well known that ferroelectrics are typical materials that possess intrinsic built-in electric field caused by spontaneous polarization.[8] Considering the simple preparation method and inherent internal electric field property of ferroelectrics, their photocatalytic properties have been studied experimentally as promising photocatalysts.[7,18-24]

Although the built-in electric field can separate photo-induced carriers, a static electric field can be easily saturated by free carries, and the enhancement of the photocatalysis, thus, is halted.[7] Therefore, in order to keep the photo-induced carriers separation incessantly during photocatalysis process, the extraction of photo-induced carriers, that is, making them transfer to the active sites at semiconductor surface to initiate the PCO processes, is equally important. Noble metals (particularly Pt) can be the electron trapping centres through the formation of a Schottky junction with the semiconductor photocatalyst, thus make these electrons to involve in catalysis more effectively.[5,25-27] Therefore, in order to promote the photo-induced carriers extraction efficiency, loading noble

[a] CAS Key Laboratory of Design and Assembly of Functional Nanostructures & Fujian Provincial Key Laboratory of Nanomaterials, Fujian Institute of Research on the Structure of Matter, Chinese Academy of Sciences, Fuzhou 350002, China.*E-mail: zhiguo@fjirsm.ac.cn
[b] Institute of Nanoscience and Nanotechnology, College of Physical Science and Technology, Central China Normal University, Wuhan 430079, China.
[c] University of Chinese Academy of Sciences, Beijing 100049, China

†Electronic Supplementary Information (ESI) available: Experimental details of EPR test, TON calculation as well as additional FE-SEM, TEM, photocatalytic cyclic test, UV-Vis, PL, and EPR data. See DOI: 10.1039/x0xx00000x

View Article Online
DOI: 10.1039/C7TA04114A

metals is an efficient approach. However, most conventional support and metal nanoparticles (NPs) are structurally non-uniform and have weak interaction between them, which is not good for photo-induced carriers extraction.[28] Inducing strong metal–support interactions (SMSI) state in the supported catalyst system will greatly facilitate the electron transfer between metal NPs and the oxide support.[25,29]

As a typical ferroelectric material, tungsten bronze-type $KSr_2Nb_5O_{15}$ (KSNO) has been widely investigated as ferroelectric and piezoelectric materials.[30] What's more, KSNO is a unipolar ferroelectric with spontaneous polarization along the c axis,[30] thus having built-in electric field along [001] direction and is a potential candidate for photocatalytic aplication.[22] Herein, a molten salt synthesis method was used for preparing tungsten bronze-type KSNO with surface oxygen vacancies, and Pt NPs were uniformly loaded on KSNO through *in situ* photodeposition method. Strong metal–support interactions were found in the KSNO/Pt catalysts which facilitates the photo-induced carriers extraction efficiency and an outstanding photocatalytic activity for ethylene oxidation was achieved.

2 Experimental sections

2.1 Preparation of $KSr_2Nb_5O_{15}$ powder photocatalysts

The $KSr_2Nb_5O_{15}$ (KSNO) powder crystals were fabricated by a molten salt synthesis (MSS) method. All reagents were analytically pure, commercially available and used without further purification. Strontium carbonate ($SrCO_3$), niobium (V) oxide (Nb_2O_5, 4 N), and potassium chloride (KCl) were used as the starting materials. In a typical preparation of tungsten bronze-type KSNO (T-KSNO): 1.8075 g Nb_2O_5 and 0.7442 g $SrCO_3$ were mixed uniformly and milled using ethanol for 2 h to obtain mixtures A. Then, 7.6551 g KCl and mixtures A were milled using ethanol for 30 min to obtain mixtures B. Then, the mixtures B were mixed by ball milling with zirconia balls as grinding media in ethanol for 10 h. The well-mixed powders were placed into an Al_2O_3 crucible, which was covered with a flat Al_2O_3 lid to prevent KCl evaporation, and then the mixtures B were calcined at high temperature for various time (e.g. 1200 °C for 6 h). After heat treatment, the products were washed several times in hot deionized water in order to remove any residual salts and then dried in air at 80 °C. Table 1 summarized the samples synthesized with different reaction time and temperatures.

2.2 Preparation of KSNO/Pt composites

The KSNO/Pt photocatalysts were prepared by the *in-situ* photoreduction method, according to the following procedure: first, the as-synthesized KSNO powder (0.3 g) and chloroplatinic acid hexahydrate ($H_2PtCl_6{\cdot}6H_2O$) (0.1545 mol/L, 24.9, 50.0, 75.2 and 100.5 µL, respectively) were dispersed in ethanol to form a stable suspension (the volume ratio of H_2O to ethanol equals 7:3). Then the suspension was stirred in dark for more than 6 h. Subsequently, the suspension was irradiated under simulated solar light for 3 h. After that, the suspension was centrifugated, washed in ethanol and water for several times. Finally, the product was dried in an oven at 60 °C. To confirm the practical content of loaded Pt, we did a series of ICP-OES analysis of (T-KSNO)/Pt samples. The actual loaded Pt contents of 0.25, 0.5, 0.75, and 1.0 wt % Pt/(T-KSNO) samples are 0.222, 0.506, 0.753, and 1.09 wt %, respectively, which are largely consistent with the nominal contents.

2.3 Physical characterization

The structure and crystallinity of the samples were investigated by X-ray diffraction (Rigaku Miniflex II) using Cu K_α (λ = 0.514178 nm) radiation (30 kV, 15 mA). A scan rate of 5° min^{-1} was applied to record the powder XRD patterns in the 2θ range of 20°–70°. The particle size and morphology of the samples were characterized on a SU-8010 field emission scanning electron microscope (FESEM) using the secondary electron imaging mode, and the accelerating voltage was 1 kV. Images of transmission electron microscopy (TEM), high-resolution transmission electron microscopy (HRTEM) were obtained using a JEM 2010 EX instrument at an accelerating voltage of 200 kV. The X-ray photoelectron spectroscopy (XPS) measurements were performed on a Phi Quantum 2000 spectrophotometer with Al Kα radiation (1,486.6 eV). The binding energies were calibrated using that of C1s (284.8 eV). Photoluminescence spectra (PL) of the photocatalysts were collected on a Varian Cary Eclipse spectrometer with an excitation wavelength of 325 nm. Electron Paramagnetic Resonance (EPR) spectra were collected on an ELEXSYS E500 spectrometer equipped with a nitrogen cryostat and the scanning temperature was around 77 K. The diffuse reflectance UV-visible spectra (UV-Vis) of the samples were recorded at room temperature using a PerkinElmer Lambda 950 UV/VIS/NIR spectrometer that was equipped with an integrating sphere covered with $BaSO_4$ as the reference. The practical Pt content in the KSNO/Pt photocatalysts was analyzed by inductively coupled plasma optical emission spectrometry (ICP-OES) technique, which was carried out on Ultima2 plasma emission spectrometer from Jobin Yvon.

2.4 Photocatalytic oxidation of C_2H_4

The photocatalytic oxidation of C_2H_4 was carried out in a homemade fixed-bed pyrex reactor of 450 ml capacity (see Fig. S1) and a flow-bed quartz reactor (28 mm×18 mm × 1 mm, see Fig. S2), respectively. All experiments were conducted at atmospheric pressure and room temperature. In a typical fixed-bed reaction: 0.2 g of the samples was dispersed uniformly on the bottom of a glass culture dish, which was placed in the bottom of the reactor. 90 µL of C_2H_4 was injected into the reactor by a micro syringe. Prior to photoirradiation,

Table 1 A summary of KSNO samples prepared at different calcination temperatures or time

Sample name	T-KSNO	KSNO-1000	KSNO-1100	KSNO-1300	KSNO-1h	KSNO-3h	KSNO-12h
Temperature/°C	1200	1000	1100	1300	1200	1200	1200
Time/h	6	6	6	6	1	3	12

View Article Online
DOI: 10.1039/C7TA04611A

the reaction system was placed in the dark for 2 h to attain the adsorption/desorption equilibrium between C_2H_4 gas and the surface of the catalyst in the reactor. At certain irradiation time intervals, 4 mL of gas was sampled from the reactor and analyzed by a gas chromatograph (GC 9720 Fuli) equipped with a HP-plot/U capillary column, a molecular sieve 13X column, a flame ionization detector (FID) and a thermal conductivity detector (TCD).

A typical flow-bed reaction proceeded was carried out as follows: the sample was placed in a quartz reactor, and then the mixed gas consisted of 78.9% N_2, 21.1% O_2 and small quantity of C_2H_4 (approximately 200 ppm) was flowed through the samples and analyzed directly by the gas chromatography (GC9720 Fuli). Before illumination, the flowing carrier gas was used to expel CO_2 and other species that adsorbed on the surface of the catalysts. During the reaction, a 300 W Xe lamp was used to provide simulated solar light.

3 Results and discussion

3.1 Structure and morphology of $KSr_2Nb_5O_{15}$ (KSNO) photocatalysts

A series of comparative experiments were carried out to investigate the growth behavior of KSNO. The crystal phases and morphologies of the as-prepared KSNO samples were established through X-ray diffraction (XRD) and field emission scanning electron microscope (FESEM), respectively. The results shown in Fig. 1 unambiguously demonstrate the changes of crystal structures along with synthetic procedures.

First, in order to determine the optimum calcination temperature, KSNO was prepared under different calcination temperatures from 1000 to 1300 °C. As shown in Fig. 1a, pure phase tungsten bronze-type KSNO (T-KSNO) was formed after calcination at 1200 °C for 6 h, which is in good agreement with the standard JCPDS card no. 34-0108. Clearly, T-KSNO samples present a smooth surface and rod-like morphology with the length up to a few microns (Fig. 2c). Moreover, the rod-like T-KSNO samples with uniform length (ca. 20 μm) can be observed in the low-magnification FESEM images (Fig. S3). We did not obtain pure phase KSNO above or below 1200 °C (Fig. 1a). When calcined at 1000 °C, KSNO is the dominant products. Impurities in the particles are $SrNb_2O_6$ (Fig. 1a KSNO-1000). Besides, the shorter rods (ca. 10 μm) with some small nanoparticles on the surface are observed in the FESEM images of KSNO-1000, as shown in Fig. 2a, further indicating the impurity in the samples. Unexpectedly, at the temperature of 1100 °C, the KSNO-1100 samples present the shortest rod-like morphology (ca. 5 μm) but with a smooth surface (Fig. 2b). Through XRD analysis (Fig. 1a KSNO-1100), we find that the KSNO-1100 samples include $SrNb_2O_6$ and $Sr_2Nb_2O_7$ besides KSNO. Increasing the calcination temperature to 1300 °C, the formation rate of $Sr_5Nb_5O_{15}$ impurity was accelerated (Fig. 1a KSNO-1300), and we obtained more and bigger $SrNb_2O_6$ impurities indicating the calcination temperature plays an important role in the reaction process. Fig. 2d shows that a number of micrometer-scale irregular bulks ($SrNb_2O_6$) and

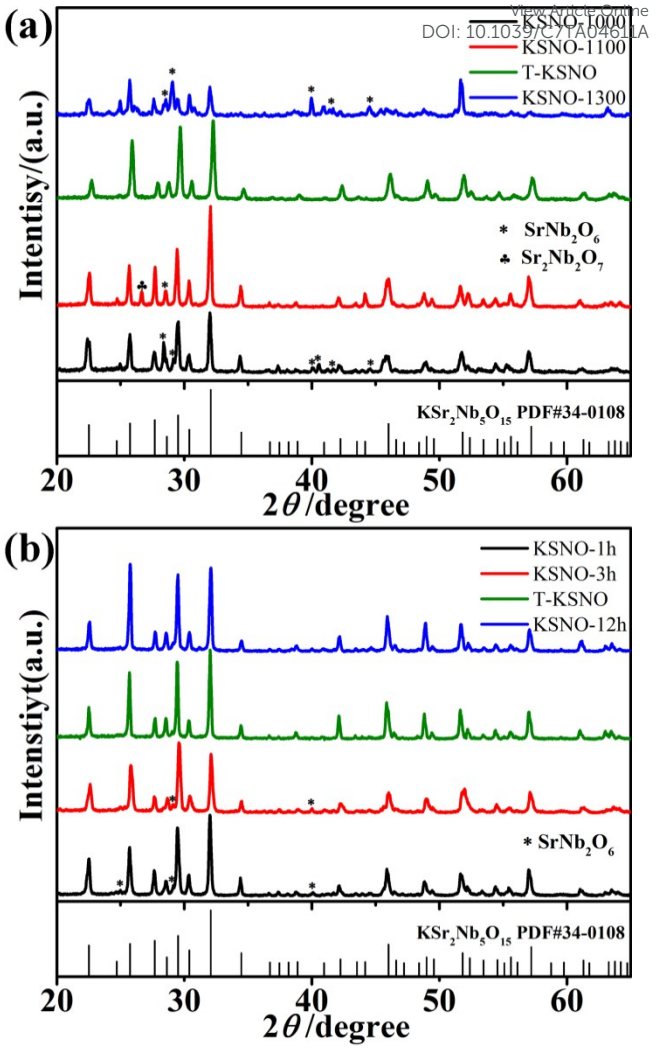

Fig. 1 XRD patterns of the KSNO samples prepared at different reaction temperatures (a) and time (b) referencing **Table 1**.

larger rod-like morphology (KSNO) are clearly observed in the KSNO-1300 sample. Thus, calcinated at 1200 °C for 6 h represents an optimum condition to prepare the tungsten bronze-type KSNO.

These results combined with literature helped us analyze the reaction mechanism for the formation of KSNO. The possible morphology evolution process of KSNO rods at different reaction temperatures is shown in Fig. 3.

As previously reported,[31-33] $SrCO_3$ decomposes at low temperature (550–650 °C), which results in the formation of SrO (reaction 1), and $SrNb_2O_6$ is the first compound to be formed (reaction 2) by the following reactions:

$$SrCO_3 \rightarrow SrO + CO_2 \uparrow \quad (1)$$

$$SrO + Nb_2O_5 \rightarrow SrNb_2O_6 \quad (2)$$

Further reaction takes place between $SrNb_2O_6$ and KCl at higher temperature (approximately 800 °C). KCl behaves as both a molten salt liquid and the K^+ source for KSNO formation. KSNO possibly forms by reaction 3:

$$5SrNb_2O_6 + 2KCl \rightarrow 2KSr_2Nb_5O_{15} + SrCl_2 \quad (3)$$

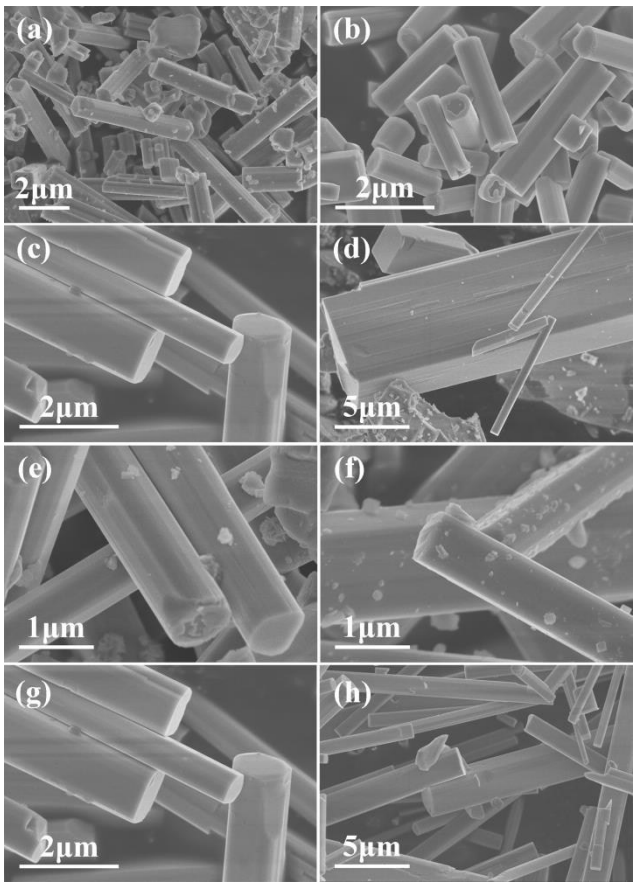

Fig. 2 FESEM images of the KSNO samples prepared at different reaction temperature and time referencing **Table 1**: (a) KSNO-1000, (b) KSNO-1100, (c) T-KSNO, (d) KSNO-1300, (e) KSNO-1h, (f) KSNO-3h, (g) T-KSNO, (h) KSNO-12h.

In addition, $Sr_2Nb_2O_7$ would be formed resulting from the superabundant $SrNb_2O_6$, if reaction 3 didn't consume $SrNb_2O_6$ timely. The following reactions may take place on the basis of reaction 1 and 2:

$$2SrNb_2O_6 + 2SrCl_2 + O_2 \rightarrow 2Sr_2Nb_2O_7 + 2Cl_2\uparrow \quad (4)$$

$$SrNb_2O_6 + SrO \rightarrow Sr_2Nb_2O_7 \quad (5)$$

At 1000 °C, reaction 4 and 5 are difficult to take place under such condition. The rate of reaction 3 is not fast enough to completely consume the $SrNb_2O_6$. Therefore, the products of KSNO-1000 samples are rod-like KSNO and $SrNb_2O_6$ nanopaticles (Fig. 2a). At 1100 °C, the rate of reaction 1 and 2 become faster, this accelerates the reaction 4 and 5 and facilitates generating bigger $SrNb_2O_6$. Consequently, we obtained rod-like KSNO, $SrNb_2O_6$ and $Sr_2Nb_2O_7$ (Fig. 2b). At 1200 °C, the rate of reaction 1 and 2 reaches equilibrium with reaction 3, as a result, pure phase KSNO was obtained. When further increasing temperature to 1300 °C, the rate of reaction 3 would be faster, then bigger KSNO was obtained (Fig. 2d). Nevertheless, the loss of KCl is accelerated at higher temperature. Meanwhile, the reaction 3 is limited with the loss of KCl. Then the reaction balance is broken. As a result, more micrometre-scale irregular bulks ($SrNb_2O_6$) and larger rod-like morphology (KSNO) were obtained.

Meanwhile, to investigate the process of KSNO crystal growth, we fixed the calcination temperature at 1200 °C and changed the reaction time to 1 h, 3 h, 6 h and 12 h,

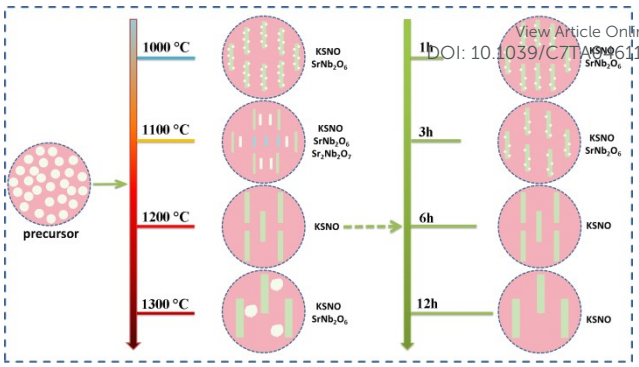

Fig. 3 Schematic illustration for the morphology evolution process of the KSNO rods.

respectively. The pure phase KSNO was obtained after 6 h of reaction, as shown in the XRD patterns (Fig. 1b). As a by-product, $SrNb_2O_6$ was detected after 1 and 3 h of reaction (Fig 1b), further indicating that reaction 1 and 2 are the first stage. Fig. 2e-h show the representative FESEM images of the samples prepared with different reaction time. As presented in the images, all the KSNO are rod-like morphology. Representative low-magnification FESEM images of the samples are shown in Fig. S3. It could be clearly observed that the length of KSNO samples grow longer with the increase of reaction time.

Similarly, the possible morphology evolution process under different reaction time at 1200 °C is shown in Fig. 3. For 1h and 3h, the reaction 3 doesn't react completely, so we obtained rod-like KSNO and $SrNb_2O_6$ nanopaticles. For 6h and 12h, pure rod-like KSNO was obtained. In addition, longer KSNO samples were achieved with the increase of reaction time, further indicating that the KSNO is growing along the certain direction.

3.2 Photocatalytic performance of KSNO and KSNO/Pt photocatalysts

Photocatalytic ethylene (C_2H_4) oxidation activities of KSNO and KSNO with Pt decoration (KSNO/Pt) samples were investigated under simulated solar light irradiation with both fixed-bed and flow-bed mode (Fig. S1 and S2). The original time-courses data of the C_2H_4 photooxidation over the as synthesized samples under the fixed-bed mode are shown in Fig. 4. To evaluate the photoreactivity quantitatively, the reaction rate constants were deduced from the Langmuir–Hinshelwood model, and the results are presented in Fig. S4. KSNO without the cocatalysts decoration exhibits very low photocatalytic activity for ethylene oxidation, and for comparison purposes, the blank experiment without any catalysts does not possess any activity under simulated sunlight illumination (Fig. 4a). By strong contrast, the photocatalytic activity of KSNO is enhanced markedly by loading Pt. As shown in Fig. 4b, 0.75 wt % Pt loading exhibits an extraordinarily high photocatalytic performance, with the reaction rate constant of 1.21 min^{-1}, which is the highest in comparison with our previous studies.[34-36] This could be largely attributed to the fact that intimately attached Pt metal as a co-catalyst, not only can efficiently trap the photogenerated electrons, but also provides effective

View Article Online
DOI: 10.1039/C7TA04614A

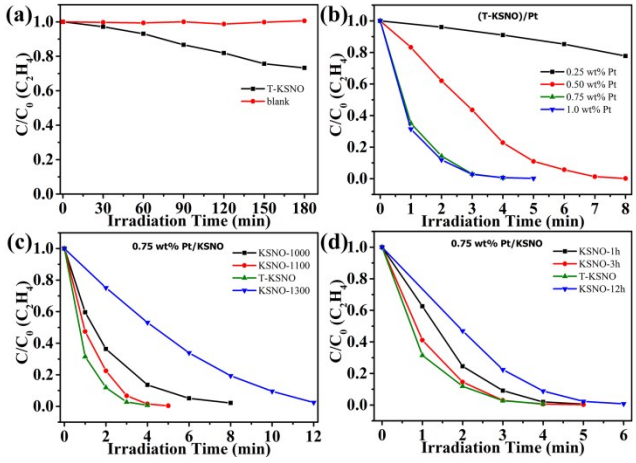

Fig. 4 Time courses of C_2H_4 photo-oxidation: upon synthesized T-KSNO samples and without catalyst (blank test) (a); upon T-KSNO samples with different Pt loading (b); upon 0.75 wt% Pt loaded KSNO samples (c, d) that sintered at the conditions referencing **Table 1.**

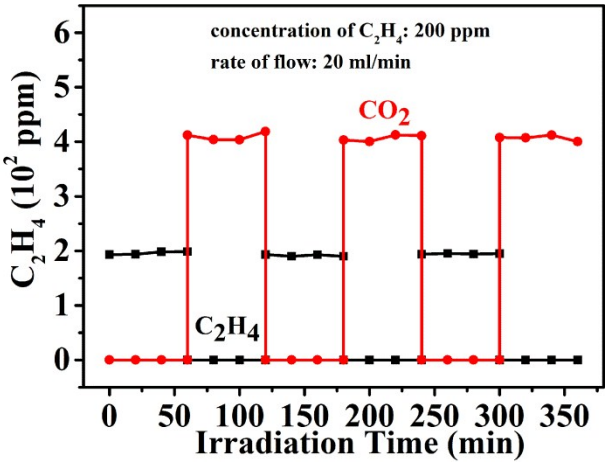

Fig. 5 Photo-oxidation of C_2H_4 and CO_2 generation on the 0.75 wt % Pt/(T-KNSO) in a flow mode.

active sites, so that it can repel the photo-excited electrons toward the bulk region, creating an electron depletion layer at the surface.[22,37,38] As seen from the photoluminescence (PL) spectra shown in Fig. S5, the fluorescence intensity decreased after loading Pt on the T-KSNO samples, which may be caused by a lower recombination rate of photogenerated electron–hole pairs in (T-KSNO)/Pt photocatalyst. The PL emission bands at around 400 and 545 nm are observed, which can be assigned to the emission of the band gap transition and charge transfer transition of an oxygen vacancy trapped electron, respectively.[39] Furthermore, the Pt loading significantly increases the visible light absorption of T-KSNO, as shown in Fig. S6. However, the activity is hardly increased further when the content of Pt is above 0.75 wt % (Fig. 4b), because excess Pt metal may easily encounter delocalized holes at KSNO semiconductors, resulting in inefficient separation of photogenerated electrons and holes.[40] The photocatalytic activity of different KSNO samples loaded the same content Pt (0.75 wt %) were also investigated (Fig. 4c and d). As expected, the (T-KSNO)/Pt photocatalysts exhibit the best performance. Because the $SrNb_2O_6$ nanaoparticles on the surface of KSNO may not only become the recombination centers of photocarriers, but also decrease photocatalytic active sites provided by Pt.

To examine the mineralization ratio of ethylene oxidation, we further conducted the ethylene oxidation reaction over the (T-KSNO)/Pt sample with a flow mode (Figure S2). As shown in Fig. 5, when the light was turned on, the concentration of C_2H_4 decreased rapidly to zero. At the same time, the concentration of CO_2 promptly increased to approximately 400 ppm. When the light was turned off, the amount of CO_2 rapidly decreased to zero, and the amount of C_2H_4 returned to the constant starting value (ca. 200 ppm). The generation of CO_2 was basically in line with the degradation of C_2H_4 and no other carbon-containing species were detected. The mineralization ratio of ethylene is determined to be ca. 100% in this reaction. To further investigate the stability of (T-KSNO)/Pt, the test of cycle reactions was examined. As shown in Fig. S7, the photocatalytic activity is highly stable after ten cyclic C_2H_4 photo-oxidation reactions. The turnover number for ethylene photo-oxidation is determined to be 2.216 (see 'Turnover number calculations' in the ESI†), indicating that the reaction is truly driven by a catalytic process.

3.3 Structural analysis of (T-KSNO)/Pt and photocatalytic mechanism

To confirm the distribution of platinum nanoparticles (Pt NPs) on the surface of T-KSNO, as-prepared 0.75 wt % Pt/(T-KSNO) was characterized by FESEM, transmission electron microscopy (TEM) and high resolution TEM (HRTEM). Fig. S8 shows the FESEM images of (T-KSNO)/Pt samples, indicating that the Pt NPs are highly dispersed on the surface of T-KSNO, which is consistent with the low-magnification TEM images, shown in Fig. S9. We randomly chose two microrods of (T-KSNO)/Pt samples, and the TEM images were shown in Fig. 6 and Fig. S9. HRTEM images in Fig. 6a and b are taken from the red circle area of Fig. S9b and d, respectively. HRTEM images further verify that the Pt NPs (ca. 2-4nm) are intimately loaded on the surface of T-KSNO. Notably, Pt NPs (Fig. 6a) or even clusters (Fig. 6b) are observed on (T-KSNO)/Pt samples. The characteristic lattice spacing of 0.396 nm corresponds to (001) facet of KSNO and 0.223-0.225 nm corresponds to (111) plane of cubic Pt, respectively.[31,41-43] The results also indicate that the KSNO particles are growing along the [001] direction, which is consistent with the previous reports.[31]

To further examine the surface bonding state and the composition of the as-prepared (T-KSNO)/Pt samples, X-ray photoelectron spectroscopy (XPS) was performed (Fig. S10). Fig. 7a and b show the XPS Pt 4f spectra of the (T-KSNO)/Pt photocatalysts before and after the catalytic testing. The spectra were deconvoluted using a standard peak-fitting technique with a few Gaussian–Lorentzian curves. The theoretical intensity ratio was 1.33, and the peak separation of 3.3 eV was used for the spin-orbit doublet $Pt4f_{7/2}$–$Pt4f_{5/2}$.[44]

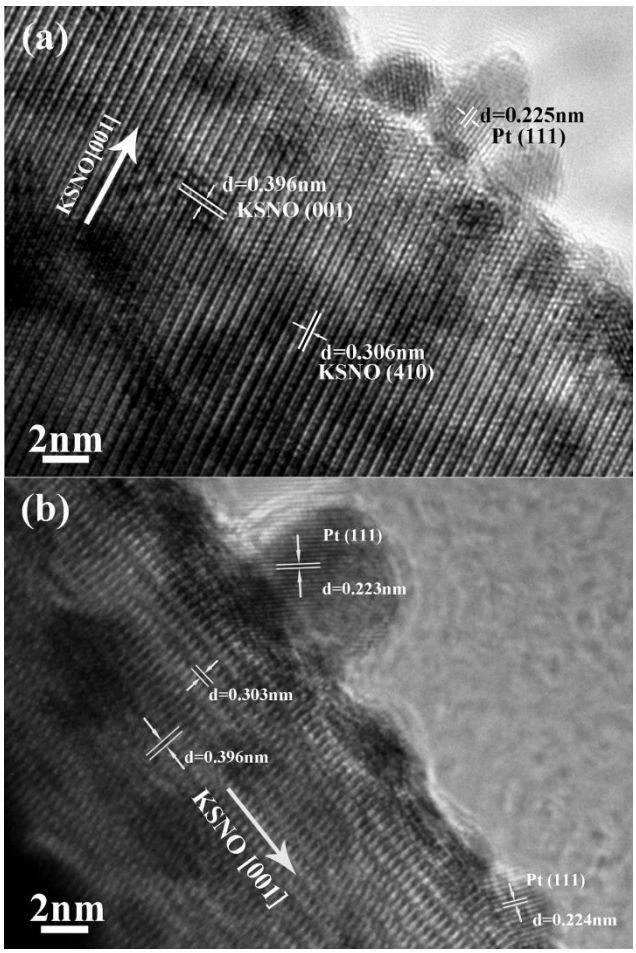

Fig. 6 HRTEM images of (T-KSNO)/Pt (0.75 wt %): (a) and (b) are taken from the red circle area of Fig. S9b and d, respectively.

Before performing the catalytic test, the spectra of fresh (T-KSNO)/Pt photocatalyst can be described by three Pt 4f doublets with the Pt $4f_{7/2}$ binding energies near 70.0, 71.6 and 74.22 eV (Fig. 7a), further indicating the successful deposition of trace Pt. It is important to note that, the first Pt 4f doublet, with the binding energy near 70.0 eV (Fig. 7a), is shifted to lower binding energy as compared to the most common value measured for bulk metallic Pt.[44-47] Such negative shifts can be explained by the electron transfer from T-KSNO to Pt. It means that the state of platinum may be described as a very electron-rich state $Pt^{\delta-}$.[44,47,48] This is attributed to the specific strong interaction between Pt and T-KSNO, which is known as "strong metal support interaction".[27,47] The second doublet located at the Pt $4f_{7/2}$ binding energies of 71.6 eV, results most probably from platinum in its oxidized state like Pt^{1+}, which is in agreement with the literatures.[44,48] The third weak doublet, with the $Pt4f_{7/2}$ binding energy near 74.2 eV corresponds to the Pt^{4+} state.[49]

A reasonable change of Pt 4f spectra can be observed in (T-KSNO)/Pt photocatalyst after its catalytic testing (Fig. 7b). The location of all peaks remains invariant, however, it should be noted that the peak intensity of $Pt^{\delta-}$ has been markedly increased. This suggests the electron transfer from T-KSNO to Pt during photocatalytic process and further proved the

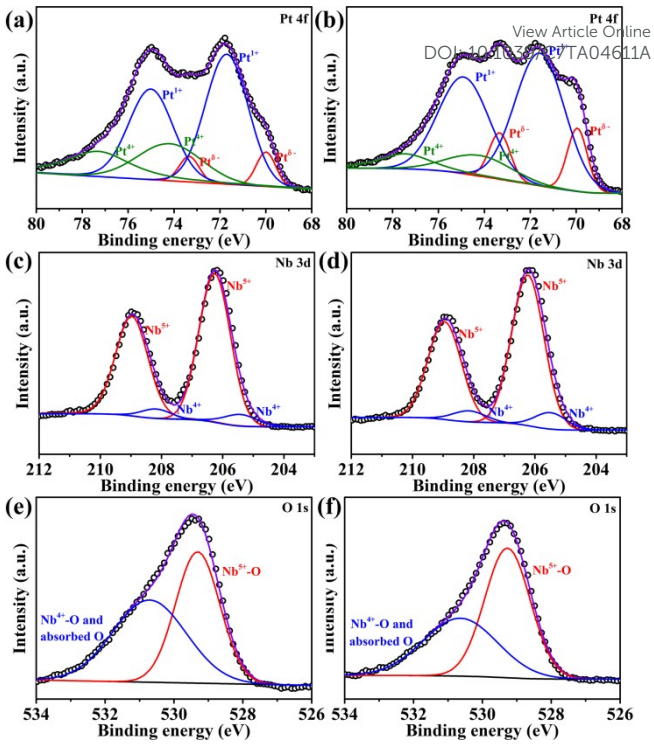

Fig. 7 XPS spectra of the (T-KSNO)/Pt (0.75 wt %) sample for before (a, c, e)and after (b, d, f) the photocatalytic reaction.

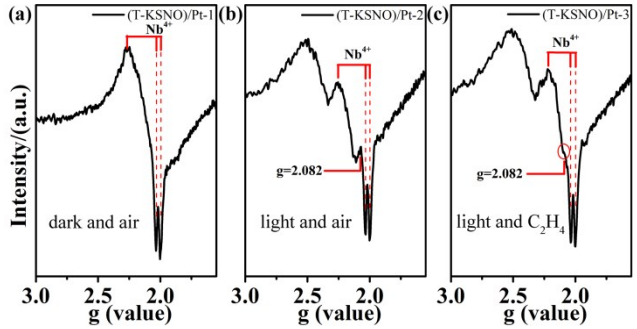

Fig. 8 EPR spectra collected upon the (T-KSNO)/Pt (0.75 wt %) sample at 77 K under various conditions: dark and air (a); under irradiation and air (b); under irradiation and inject C_2H_4 (c).

formation of strong metal support interaction state in (T-KSNO)/Pt photocatalyst. We suppose both the built-in electric field in the T-KSNO and the excellent contact between T-KSNO and Pt account for the formation of strong metal support interaction herein.

Beyond that, the unaltered Nb 3d spectra (before and after reaction) were shown in Fig. 7c and d. The theoretical intensity ratio was 1.5, and the peak separation of 2.7 eV was used for the spin-orbit doublet $Nb3d_{5/2}$–$Nb3d_{3/2}$. The doublet located at 206.2 eV (Fig. 7c and d) is attributed to the $Nb3d_{5/2}$ peak of Nb^{5+} in NbO_6 octahedra.[50,51] The lower binding energy peak located at 205.4 eV is the $Nb3d_{5/2}$ peak of Nb^{4+} in highly distortional NbO_6 octahedral, which may indicate the formation of oxygen vacancies.[52-54] This would be further confirmed by the result of XPS O1s spectra and electron paramagnetic resonance (EPR). As shown in O1s spectra (Fig.

View Article Online
DOI: 10.1039/C7TA04611A

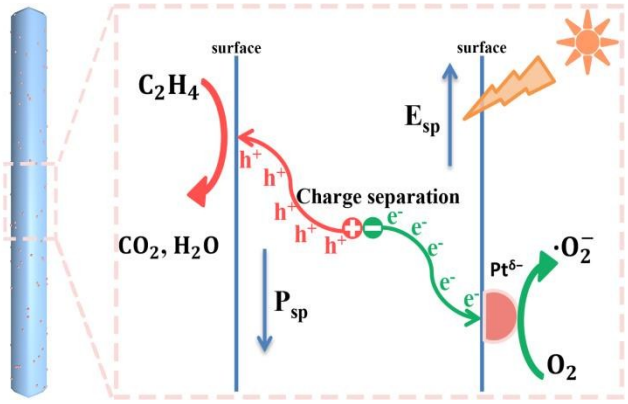

Fig. 9 Schematic illustration of charge separation and extraction in the (T-KSNO)/Pt sample and associated photo-oxidation of C_2H_4. P_{sp} is the polarization and E_{sp} is the internal electric field.

7e and f), the two peaks located at binding energies of 529.3 and 530.4 eV can be observed, which could be attributed to lattice oxygen in the normal NbO_6 octahedral, and highly distortional NbO_6 octahedral (Nb^{4+}-O) leaded by oxygen vacancy or adsorbed oxygen, respectively.[55-57]

In order to further confirm our hypothesis about electron transfer pathway within this (T-KSNO)/Pt catalytic reaction system, we performed electron paramagnetic resonance (EPR) studies. The detailed experimental method and the schematic illustration of EPR test process is shown in Fig. S11. EPR is a powerful tool for investigating paramagnetic species with, at least, one unpaired electron.[58] Platinum with unpaired electronic state possesses paramagnetism, which has been detected through EPR in previous literature.[59,60] Fig. 8 shows the low temperature EPR spectra (at ca. 77K) collected on the (T-KSNO)/Pt sample under various conditions. Under the dark and air atmosphere, the fresh sample shows the signal that corresponds to electrons delocalized at highly distorted surface NbO_6 octahedral sites, for the presence of Nb^{4+}.[61-63] It can be clearly seen that, simulated solar light irradiation of this sample creates distinctive signals (Fig. 8b), assigned to paramagnetic species Pt ($Pt^{\delta-}$, g=2.082), which is consistent with the previous reports.[59,60] This result further indicates the electrons transferred from T-KSNO to Pt, as a result, the paramagnetic species Pt is formed. Understandably, after C_2H_4 was injected into the reactor, the signal of $Pt^{\delta-}$ (g=2.082) almost disappeared, as shown in Fig. 8c, indicating that the PCO process consumed the transferred electrons. In contrast, the EPR spectra of T-KSNO sample show almost no change under the same experimental method (Fig. S12).

Based on the above analysis, the transfer of photo-induced carriers during the PCO process upon the (T-KSNO)/Pt catalyst is described in Fig. 9. Firstly, when the catalyst is irradiated by simulated solar light, photo-induced electron–hole pairs are formed and then separated by the internal electric field caused by the spontaneous polarization along c-axis.[30] Subsequently, the photo-induced electrons transfer to Pt nanoparticles, which are used as the electron trapping centres, and then participate in PCO reaction. It is the formation of strong metal-support interaction (SMSI) state that drives the photo-generated electrons to transfer toward Pt nanoparticles instead of along the c-axis.

Conclusions

In summary, we have successfully synthesized tungsten bronze-type KSNO with surface oxygen vacancies via molten salt synthesis method. The growth behaviour of KSNO was investigated by varying the calcination temperature and synthesis duration, and then a possible morphology evolution process was proposed. More importantly, we reported a novel (T-KSNO)/Pt photocatalyst that synthesized by *in situ* photodeposition method processes strong metal–support interactions which significantly facilitates the photo-induced carriers extraction efficiency. A remarkably enhanced photocatalytic activity for ethylene oxidation over (T-KSNO)/Pt has been demonstrated, which shows excellent stability as well. Further in-depth studies of this material with different potential applications in the field of photocatalysis are being under way.

Acknowledgements

This work was financially supported by the National Key Project on Basic Research (Grant No. 2013CB933203), the Strategic Priority Research Program of the Chinese Academy of Sciences (Grant No. XDB20000000), the Natural Science Foundation of China (Grant No. 21373224, 21577143, 51502289 and 21607153), the Natural Science Foundation of Fujian Province (2015J05044 and 2017J05031) and the Key Project of Frontier Science of the Chinese Academy of Sciences (QYZDB-SSW-JSC027).

Notes and references

1 N. Keller, M. N. Ducamp, D. Robert and V. Keller, Chem Rev, 2013, 113, 5029-5070.
2 A. H. Mamaghani, F. Haghighat and C.-S. Lee, Applied Catalysis B: Environmental, 2017, 203, 247-269.
3 J. Mo, Y. Zhang, Q. Xu, J. J. Lamson and R. Zhao, Atmospheric Environment, 2009, 43, 2229-2246.
4 Y. Qu and X. Duan, Chem Soc Rev, 2013, 42, 2568-2580.
5 S. Bai, J. Jiang, Q. Zhang and Y. Xiong, Chem Soc Rev, 2015, 44, 2893-2939.
6 M. G. Kibria, F. A. Chowdhury, S. Zhao, B. AlOtaibi, M. L. Trudeau, H. Guo and Z. Mi, Nat Commun, 2015, 6, 6797.
7 H. Li, Y. Sang, S. Chang, X. Huang, Y. Zhang, R. Yang, H. Jiang, H. Liu and Z. L. Wang, Nano Lett, 2015, 15, 2372-2379.
8 L. Li, P. A. Salvador and G. S. Rohrer, Nanoscale, 2014, 6, 24-42.
9 P. Wadhwa, B. Liu, M. A. McCarthy, Z. Wu and A. G. Rinzler, Nano Lett, 2010, 10, 5001-5005.
10 D. Mongin, E. Shaviv, P. Maioli, A. Crut, U. Banin, N. Del Fatti and F. Vallée, ACS Nano, 2012, 6, 7034-7043.
11 J. Tian, Y. Sang, G. Yu, H. Jiang, X. Mu and H. Liu, Adv Mater, 2013, 25, 5075-5080.
12 J. Li, L. Cai, J. Shang, Y. Yu and L. Zhang, Adv Mater, 2016, 28, 4059-4064.
13 X. Fan, J. Liu, K. Lai and C. Wang, Applied Catalysis B: Environmental, 2017, 206, 599-607.

14 H. He, J. Yin, Y. Li, Y. Zhang, H. Qiu, J. Xu, T. Xu and C. Wang, Applied Catalysis B: Environmental, 2014, 156-157, 35-43.
15 X. Fan, L. Zang, M. Zhang, H. Qiu, Z. Wang, J. Yin, H. Jia, S. Pan and C. Wang, Chemistry of Materials, 2014, 26, 3169-3174.
16 L. Jiang, Y. Zhang, Y. Qiu and Z. Yi, RSC Adv., 2014, 4, 3165-3170.
17 X. Chen, Y. Li, X. Pan, D. Cortie, X. Huang and Z. Yi, Nat Commun, 2016, 7, 12273.
18 J. L. Giocondi and G. S. Rohrer, J. Phys. Chem. B, 2001, 105, 8275-8277.
19 A. Kakekhani and S. Ismail-Beigi, J. Mater. Chem. A, 2016, 4, 5235-5246.
20 S. Park, C. W. Lee, M. G. Kang, S. Kim, H. J. Kim, J. E. Kwon, S. Y. Park, C. Y. Kang, K. S. Hong and K. T. Nam, Phys Chem Chem Phys, 2014, 16, 10408-10413.
21 M. Stock and S. Dunn, The Journal of Physical Chemistry C, 2012, 116, 20854-20859.
22 P. Wang, L. Schwertmann, R. Marschall and M. Wark, J. Mater. Chem. A, 2014, 2, 8815.
23 Y. Zhang, A. M. Schultz, P. A. Salvador and G. S. Rohrer, J. Mater. Chem., 2011, 21, 4168.
24 J. Cao, Y. Ji, C. Tian and Z. Yi, Journal of Alloys and Compounds, 2014, 615, 243-248.
25 Q. Liu, Y. Chai, L. Zhang, J. Ren and W.-L. Dai, Applied Catalysis B: Environmental, 2017, 205, 505-513.
26 S. Naya, M. Teranishi, K. Kimura and H. Tada, Chem Commun (Camb), 2011, 47, 3230-3232.
27 S. J. Tauster, S. C. Fung, R. T. K. Baker and J. A. Horsley, Science, 1981, 211, 1121-1125.
28 B. Zhang, X.-W. Guo, H. Liang, H. Ge, X. Gu, S. Chen, H. Yang and Y. Qin, ACS Catalysis, 2016, 6, 6560-6566.
29 P. Chen, A. Khetan, F. Yang, V. Migunov, P. Weide, S. P. Stürmer, P. Guo, K. Kähler, W. Xia, J. Mayer, H. Pitsch, U. Simon and M. Muhler, ACS Catalysis, 2017, 7, 1197-1206.
30 S. Alkoy, C. Duran and D. A. Hall, Journal of the American Ceramic Society, 2008, 91, 1597-1602.
31 L. Liu, F. Gao, G. Hu and J. Liu, Powder Technology, 2013, 235, 806-813.
32 Z. Yang, L. Wei and Y. Chang, Journal of the European Ceramic Society, 2007, 27, 267-272.
33 L. Zhao, F. Gao, C. Zhang, M. Zhao and C. Tian, Journal of Crystal Growth, 2005, 276, 446-452.
34 Y. Li, Y. Cai, X. Chen, X. Pan, M. Yang and Z. Yi, RSC Adv., 2016, 6, 2760-2767.
35 X. Pan, X. Chen and Z. Yi, ACS Appl Mater Interfaces, 2016, 8, 10104-10108.
36 P. Long, Y. Zhang, X. Chen and Z. Yi, J. Mater. Chem. A, 2015, 3, 4163-4169.
37 J. Zhang, Z. Yu, Z. Gao, H. Ge, S. Zhao, C. Chen, S. Chen, X. Tong, M. Wang, Z. Zheng and Y. Qin, Angew Chem Int Ed Engl, 2017, 56, 816-820.
38 P. Wang, F. Sun, J. H. Kim, J. H. Kim, J. Yang, X. Wang and J. S. Lee, Phys Chem Chem Phys, 2016, 18, 25831-25836.
39 Y. Cong, J. L. Zhang, F. Chen and M. Anpo, J. Phys. Chem. C, 2007, 111, 6976-6982.
40 Y.-C. Chen, Y.-C. Pu and Y.-J. Hsu, The Journal of Physical Chemistry C, 2012, 116, 2967-2975.
41 C. Wang, H. Daimon, T. Onodera, T. Koda and S. Sun, Angew Chem Int Ed Engl, 2008, 47, 3588-3591.
42 Y. Bing, H. Liu, L. Zhang, D. Ghosh and J. Zhang, Chem Soc Rev, 2010, 39, 2184-2202.
43 A. Feoktistov, V. G. Golubev, J. L. Hutchison, D. A. Kurduykov, B. Pevtsov, V. V. Ratnikov, J. Sloan and L. M. Sorokin, Semicond. Sci. Technol., 2001, 16, 955-960.
44 E. A. Kozlova, T. P. Lyubina, M. A. Nasalevich, A. V. Vorontsov, A. V. Miller, V. V. Kaichev and V. N. Parmon, Catalysis Communications, 2011, 12, 597-601.
45 V. V. Narkhede, A. De Toni, V. S. Narkhede, M. Reichinger, A. Birkner, J. W. Niemantsverdriet, W. Grünert and H. Gies, Journal of Materials Science, 2009, 44, 6701-6709.
46 L. Wang, X. Lu, C. Wen, Y. Xie, L. Miao, S. Chen, H. Li, P. Li and Y. Song, J. Mater. Chem. A, 2015, 3, 608-616.
47 H. Tada, F. Suzuki, S. Ito, T. Akita, K. Tanaka, T. Kawahara and H. Kobayashi, J. Phys. Chem. B, 2002, 106, 8714-8720.
48 C. R. Lederhos, J. M. Badano, M. E. Quiroga, A. E. Ramirez, J. J. Martinez and H. A. Rojas, Curr. Org. Chem., 2012, 16, 2782-2790.
49 G. Sivalingam, K. Nagaveni, M. S. Hegde and G. Madras, Applied Catalysis B: Environmental, 2003, 45, 23-38.
50 S. Lanfredi, D. H. M. Gênova, I. A. O. Brito, A. R. F. Lima and M. A. L. Nobre, Journal of Solid State Chemistry, 2011, 184, 990-1000.
51 A. R. F. Lima, J. C. Sczancoski, M. Siu Li, E. Longo and E. R. Camargo, Ceramics International, 2016, 42, 4709-4714.
52 G. Zhang, X. Zou, J. Gong, F. He, H. Zhang, S. Ouyang, H. Liu, Q. Zhang, Y. Liu, X. Yang and B. Hu, Journal of Molecular Catalysis A: Chemical, 2006, 255, 109-116.
53 H. Dong, G. Chen, J. Sun, Y. Feng, C. Li and C. Lv, Chem Commun (Camb), 2014, 50, 6596-6599.
54 J. Jeong, N. Aetukuri, T. Graf, T. D. Schladt, M. G. Samant and S. S. P. Parkin, Science, 2013, 339, 1402-1405.
55 E. Ramos-Moore, P. Ferrari, D. E. Diaz-Droguett, D. Lederman and J. T. Evans, Journal of Applied Physics, 2012, 111, 014108.
56 Q. Zou, H. Ruda, B. G. Yacobi and M. Farrell, Thin Solid Films, 2002, 402, 65-70.
57 T. Yu, Y. F. Chen, Z. G. Liu, S. B. Xiong, L. Sun, X. Y. Chen and N. B. Ming, Mater. Lett., 1996, 26, 291-294.
58 Z. Wang, W. Ma, C. Chen, H. Ji and J. Zhao, Chemical Engineering Journal, 2011, 170, 353-362.
59 A. Kawamori, R. Aoki and M. Yamashita, Journal of Physics C: Solid State Physics, 1985, 18, 5487.
60 F. Wen-Lin, Y. Wei-Qing, Z. Wen-Chen and L. Xue-Ming, Journal of Alloys and Compounds, 2010, 507, 498-501.
61 P. Wang, N. M. Dimitrijevic, A. Y. Chang, R. D. Schaller, Y. Z. Liu, T. Rajh and E. A. Rozhkova, ACS Nano, 2014, 8, 7995-8002.
62 C. Verissimo, F. M. S. Garrido, O. L. Alves, P. Calle, A. MartinezJuarez, J. E. Iglesias and J. M. Rojo, Solid State Ion., 1997, 100, 127-134.
63 M. Lardon and H. H. Günthard, The Journal of Chemical Physics, 1966, 44, 2010-2015.

View Article Online
DOI: 10.1039/C7TA04611A

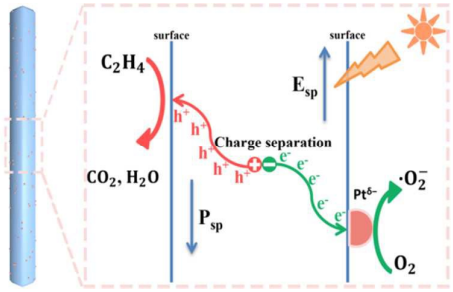

Platinum nanoparticles supported on defective tungsten bronze-type $KSr_2Nb_5O_{15}$ was shown as a novel photocatalyst for efficient oxidation of ethylene.